

Report No.
UCB/SEMM-2011/06

Structural Engineering
Mechanics and Materials

**A Time-Domain Discontinuous Galerkin
Method for Mechanical Resonator
Quality Factor Computations**

By

Sanjay Govindjee and Per-Olof Persson

June 2011

Department of Civil and Environmental Engineering
University of California, Berkeley

A Time-Domain Discontinuous Galerkin Method for Mechanical Resonator Quality Factor Computations

Sanjay Govindjee^a, Per-Olof Persson^{b,*}

^a*Department of Civil Engineering, University of California, Berkeley, Berkeley, CA 94720-1710, USA*

^b*Department of Mathematics, University of California, Berkeley, Berkeley, CA 94720-3840, USA*

Abstract

Numerical simulations are becoming increasingly important in the design of micromechanical resonators, in particular for the prediction of complex frequency response in high quality devices. This is particularly true when there is need to accurately predict damping due to anchor losses and other complex wave interactions. Frequency based approaches have been shown to predict these accurately, however, they require the solution of eigenvalue problems or the inversion of Helmholtz-type operators which are known to be very difficult for large-scale iterative solvers. We propose using a time-domain approach instead, where a broadband input signal is propagated through the system with a local explicit time-stepper. This is achieved using a high-order Discontinuous Galerkin (DG) discretization for the elasticity equations, in particular a second-order formulation with Compact DG fluxes and a Runge-Kutta time integrator, where the block-diagonal mass matrices allow for efficient and accurate time stepping. Our solver scales well on distributed parallel computers, even in three spatial dimension and for large problem sizes. The resulting output signal is analyzed using a filter diagonalization method, which is capable of finding accurate frequencies and quality factors for as little as a hundred periods of data. We validate the high-order accuracy of our scheme on model problems, and demonstrate the feasibility of our proposed analysis process on two high quality factor disk resonators, using an axisymmetric formulation as well as full three dimensional simulations.

Key words: quality factor, time-domain, discontinuous Galerkin, filter diagonalization, Helmholtz, linear elasticity, anchor loss, MEMS resonator

1. Introduction

Electromechanical resonators and filters, such as quartz, ceramic, and surface-acoustic wave devices, are important signal-processing elements in communication and sensing systems. There has been substantial progress in developing new miniaturized electromechanical resonators using micro fabrication processes (MEMS devices). These include thin-film bulk acoustic resonators (FBARs), as well as electrostatically driven and sensed lateral bending- and bulk-mode microresonators. These devices can be used both as frequency references in sensor node transceivers and as the sensing elements themselves. Resonator-based sensors have also long been recognized as an attractive approach to high-performance, low-power sensing of both physical and chemical signals. Arrays of coupled or isolated resonators are also advantageous for

* Corresponding author. Tel.: +1-510-642-6947; Fax.: +1-510-642-8204.

Email address: persson@berkeley.edu (Per-Olof Persson).

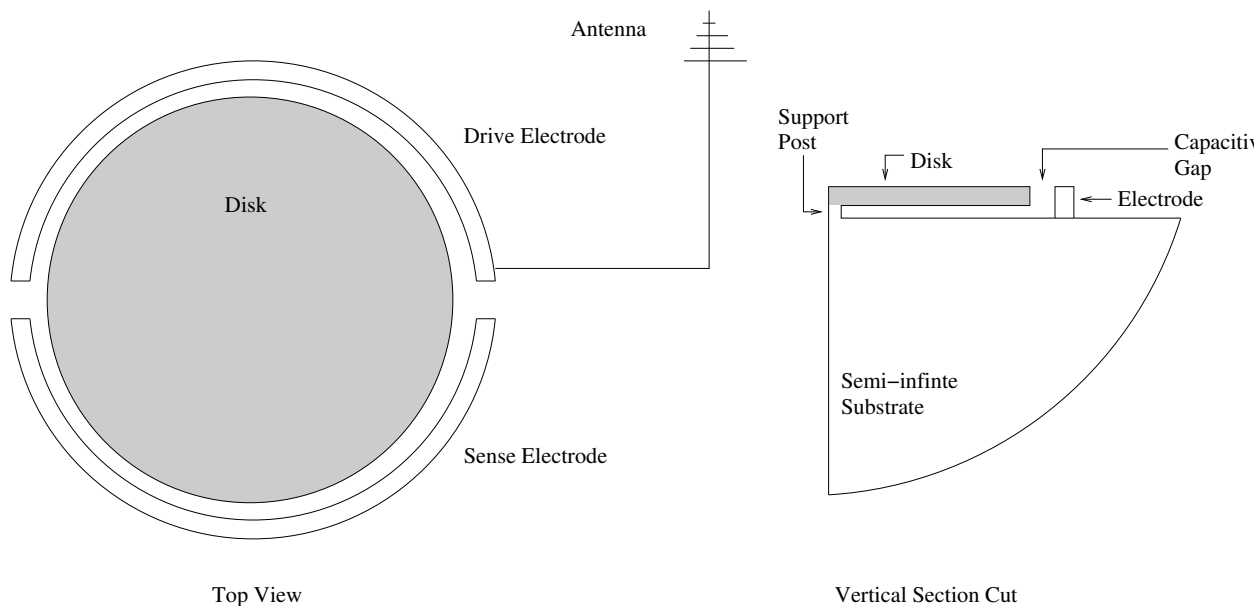


Fig. 1. Simple single disk resonator system with one drive and one sense electrode.

many signal processing and sensing applications. Experimental demonstrations of resonant quality factors, Q -factors, over 10,000 at GHz frequencies coupled to excellent thermal and aging stability, give promise that resonant micromechanical devices will be a strong and vital part of a number of future wireless communication sub-systems, from cellular handsets, to PDA's, to low-power networked sensors, to ultra-sensitive radar and jam-resistant communicators. The key to the successful operation of many such devices is the design and fabrication of microresonators and systems of resonators with very low damping characteristics – Q -factors from 10,000 to 1,000,000. This is a very demanding mechanical requirement due to the myriad sources of dissipation in these systems. Of the common loss mechanisms, anchor loss is particularly hard to predict and that is our focus in this paper.

Physically, anchor loss results from the emission of elastic energy into the substrate (chip) upon which the resonator is built. To be concrete, consider as a representative example the radial disk resonator shown schematically in Fig. 1 that is meant to operate as a signal selector. The essence of the system is a disk that vibrates and is supported on a post which is attached to a chip, that on the scale of the drawing is very well modeled as semi-infinite in extent. The disk is excited by an electrical signal that comes from, say, an antenna and is transmitted to the disk through a capacitive gap as an applied pressure on the outer edge of the disk. Those parts of the input signal that match in mode and frequency a natural vibration of the disk are then amplified as elastic vibrations by the disk. This motion can be sensed through the electrodes surrounding the disk. Considering the forces involved and typical semi-conductor materials it is clear that such a system will only be feasible if the damping is very small for the frequency of interest. In the case of anchor loss, this damping comes from the direct transport of elastic wave energy through the support post and out into the semi-infinite chip.

The essential mathematical problem in determining if a given design will work boils down to estimating the complex-valued eigenfrequencies of a device in a frequency range of interest. The real part of the eigenfrequency gives the possible operating frequency of the resonator and twice the magnitude of the imaginary part divided by the modulus of the eigenfrequency gives the damping (i.e. the inverse Q -factor). The accurate estimation of this latter quantity relies upon a good model for the semi-infinite elastic substrate. One natural path of attack would be to construct a Green function for the substrate. While formal expressions exist for such a function, they are of little practical use [1, Chap. 6]. Because of this, there has been a long line of research devoted to modeling the elastic half-space via absorbing boundary conditions; see e.g. [2–8] and references therein. For our purposes, viz. that of developing a scalable analysis methodology, we will

utilize the simplest of the existing proposals the Lysmer-Kuhlemeyer boundary damper [2] which can be thought of as an extension of the Sommerfeld radiation boundary condition to elasticity.

Once the model of the substrate is established. The remaining problem is to estimate the eigenfrequencies of the system model. The natural course is to look at the problem in the time harmonic setting and to employ an efficient eigensolver in the frequency range of interest – e.g. shift-and-invert Arnoldi style methodologies. For systems that can be modeled as two dimensional, this is an effective strategy as pointed out in [8]. For more complex three-dimensional problems, [9] has developed a parallel iterative methodology based on a Jacobi-Davidson QZ (JDQZ) algorithm [10–12] that tolerates inaccurate linear solves. The methodology scales but nonetheless still suffers from the inherent difficulties associated with inverting Helmholtz-like operators. As such, it would be impractical for the simulation of resonator-array systems as have been proposed for example by [13].

To circumvent these difficulties we propose to look instead to a time domain resolution of the problem and borrow methodologies that have been successful in related problems that arise in quantum mechanics. The methodology which we develop in the sections to follow is based upon the following 3 elements:

- (i) We excite the system of interest with a specially prepared pulse excitation.
- (ii) We evolve the dynamics of the system explicitly in time at high-space and -time accuracy in an efficient manner using a discontinuous Galerkin approximation in space and a Runge-Kutta method in time [14,15].
- (iii) We measure the system response in time (as would be done in a real driven device) and perform harmonic inversion using the filter diagonalization method of [16,17] to extract the complex-valued eigenfrequencies.

Taken as a whole we will demonstrate this yields an effective and efficient methodology for tackling the outlined class of problems. Looking ahead, we shall see that using a discontinuous Galerkin approximation will allow us to enjoy high rates of spatial convergence without the complications of slow large matrix inversions and similarly a high order Runge-Kutta method will do the same temporally. The filter diagonalization method will be seen to work effectively and efficiently for our problem class even when we are dealing with relatively short time signals, say, $O(100)$ periods.

2. Governing Equations

Microelectromechanical (MEMS) resonators are typically fabricated from single and poly-crystalline semiconductor materials such as Silicon, Germanium, etc., with polycrystalline Silicon being the most common. At working loads, such materials deform in a linear manner and thus the equations of linear elasticity provide a good description of their response characteristics. For presentation purposes we restrict our attention to the isotropic case.

2.1. 3D Equations

The equations of elasticity include the basic equations of linear and angular momentum balance, the kinematic relations, and the constitutive laws. Starting from an elastic body Ω with points $\mathbf{x} \in \Omega$, the balance of linear momentum is given by

$$\nabla \cdot \boldsymbol{\sigma}^T + \mathbf{b} = \rho \frac{\partial^2 \mathbf{u}}{\partial t^2}, \quad (1)$$

where $\rho(\mathbf{x})$ is the material density, $\mathbf{u}(\mathbf{x}, t)$ are the displacements, t is time, and $\boldsymbol{\sigma}(\mathbf{x}, t)$ is the second order tensor representing the stresses. Angular momentum balance requires $\boldsymbol{\sigma}^T = \boldsymbol{\sigma}$. The kinematic relation connects the second order strain tensor $\boldsymbol{\varepsilon}(\mathbf{x}, t)$ to the displacements as:

$$\boldsymbol{\varepsilon} = \frac{1}{2} (\nabla \mathbf{u} + \nabla \mathbf{u}^T) = \nabla^s \mathbf{u}, \quad (2)$$

where ∇^s represents the symmetric gradient operator. For isotropic materials the constitutive law is given by

$$\boldsymbol{\sigma} = 2\mu\boldsymbol{\varepsilon} + \lambda\text{tr}(\boldsymbol{\varepsilon})\mathbf{1}, \quad (3)$$

where $\mu > 0$ and $\lambda > 0$ are the Lamé parameters, $\text{tr}(\cdot)$ is the trace operator, and $\mathbf{1}$ is the second order identity tensor. In indicial form these relations are given as $\sigma_{ji,j} = \rho\partial^2 u_i / \partial t^2$, $\sigma_{ij} = \sigma_{ji}$, $\varepsilon_{ij} = (u_{i,j} + u_{j,i})/2$, and $\sigma_{ij} = 2\mu\varepsilon_{ij} + \lambda\varepsilon_{kk}\delta_{ij}$.

2.1.1. Required boundary conditions

For our problems of interest the boundary $\partial\Omega = \overline{\partial\Omega_u \cup \partial\Omega_\sigma \cup \partial\Omega_r}$, where $\partial\Omega_u$, $\partial\Omega_\sigma$, $\partial\Omega_r$ are mutually exclusive and represent the Dirichlet, Neumann, and radiation parts of the boundary, respectively. The Neumann boundary conditions are of the form

$$\boldsymbol{\sigma}^T \mathbf{n} = \bar{\mathbf{t}}, \quad (4)$$

where \mathbf{n} is the unit outward normal to $\partial\Omega_\sigma$ and $\bar{\mathbf{t}}$ are given imposed tractions. The Dirichlet boundary conditions are of the form

$$\mathbf{u} = \bar{\mathbf{u}}, \quad (5)$$

where $\bar{\mathbf{u}}$ are given displacement values. On the radiation part of the boundary we impose the Lysmer-Kuhlemeyer [2] condition

$$\boldsymbol{\sigma}^T \mathbf{n} + \mathbf{Z} \frac{\partial \mathbf{u}}{\partial t} = 0, \quad (6)$$

where $\mathbf{Z} = \rho[c_p \mathbf{n} \otimes \mathbf{n} + c_s(\mathbf{1} - \mathbf{n} \otimes \mathbf{n})]$, $c_p = \sqrt{(2\mu + \lambda)/\rho}$ is the pressure wave speed, and $c_s = \sqrt{\mu/\rho}$ is the shear wave speed. This boundary condition is a first order approximation to the out-going wave condition; it is somewhat analogous to the Sommerfeld condition that is often used in the scalar wave case.

2.1.2. Axisymmetric form

For axisymmetric problems the equations of elasticity possess a conservation-like form. In particular, the linear momentum balance equations can be written as:

$$(r\sigma_{rr})_{,r} + (r\sigma_{rz})_{,z} - \sigma_{\theta\theta} = r\rho \frac{\partial^2 u_r}{\partial t^2} \quad (7)$$

$$(r\sigma_{rz})_{,r} + (r\sigma_{zz})_{,z} = r\rho \frac{\partial^2 u_z}{\partial t^2}. \quad (8)$$

In this setting the non-zero displacement components are $u_r(r, z, t)$ and $u_z(r, z, t)$, where r and z are radial and vertical coordinates and the relevant strains are $\varepsilon_{rr} = u_{r,r}$, $\varepsilon_{zz} = u_{z,z}$, $\varepsilon_{\theta\theta} = u_r/r$, and $\varepsilon_{rz} = (u_{r,z} + u_{z,r})/2$. The constitutive relations give the non-zero stresses as

$$\begin{pmatrix} \sigma_{rr} \\ \sigma_{zz} \\ \sigma_{\theta\theta} \\ \sigma_{rz} \end{pmatrix} = \begin{pmatrix} 2\mu\varepsilon_{rr} + \lambda(\varepsilon_{rr} + \varepsilon_{zz} + \varepsilon_{\theta\theta}) \\ 2\mu\varepsilon_{zz} + \lambda(\varepsilon_{rr} + \varepsilon_{zz} + \varepsilon_{\theta\theta}) \\ 2\mu\varepsilon_{\theta\theta} + \lambda(\varepsilon_{rr} + \varepsilon_{zz} + \varepsilon_{\theta\theta}) \\ 2\mu\varepsilon_{rz} \end{pmatrix}. \quad (9)$$

3. Discretization

Our discretization of the elasticity equations is based on a discontinuous Galerkin formulation in space, where the second-order derivatives are treated with the Compact Discontinuous Galerkin (CDG) method [15]. In time, we re-write the system as a first-order system and use a standard explicit Runge-Kutta method. The main benefit with these choices is that the solver is local and only accesses neighboring element data at each residual evaluation, which in turns leads to good parallelization and scaling properties. While a standard continuous finite element method might be more appropriate for these equations, it would not be as well suited for explicit time-stepping unless the mass matrix is lumped, which would decrease the order of accuracy.

Our scheme is a completely general finite element formulation on unstructured meshes, and in particular our implementation is based on triangular and tetrahedral elements. This gives a high flexibility in terms of mesh generation and adaptation for arbitrary geometries, where a wide range of methods are capable of generating quality meshes essentially automatically [18]. For our problems, it is essential to obtain mesh elements of highest possible quality, since even a single bad one can dictate a poor CFL condition for the explicit time-stepping. Therefore, we use the DistMesh mesh generator [19], which tends to produce highly regular meshes, and a standard Delaunay-refinement based mesh generator [20] together with standard smoothing and face/edge flipping [21]. Furthermore, the mesh element sizes need to be close to constant in order to (1) resolve the constant wave lengths and (2) to avoid a bad CFL condition.

To obtain high-order accuracy from the scheme, any curved boundaries must be represented by curved elements. For this we use isoparametric elements, which represent the geometry by polynomial functions of the same degree as the approximation space for the solution. These functions are created using a standard nodal approach, where the boundary nodes of the elements are positioned on the true curved boundary and the internal nodes are distributed uniformly within the element. For our well-shaped uniform meshes, we have not seen any reason to use global mesh curving schemes [22].

3.1. Spatial Discretization

3.1.1. Compact DG formulation

For the space discretization we denote the elements of the mesh by $\mathcal{T}_h = \{K\}$ which subdivide the physical domain Ω , and we introduce the finite element spaces \mathcal{V}_h^p and Σ_h^p as:

$$\mathcal{V}_h^p = \{\mathbf{v} \in [L^2(\Omega)]^3 \mid \mathbf{v}|_K \in [\mathcal{P}_p(K)]^3 \forall K \in \mathcal{T}_h\}, \quad (10)$$

$$\Sigma_h^p = \{\boldsymbol{\tau} \in [L^2(\Omega)]^{3 \times 3} \mid \boldsymbol{\tau}|_K \in [\mathcal{P}_p(K)]^{3 \times 3} \forall K \in \mathcal{T}_h\}, \quad (11)$$

where $\mathcal{P}_p(K)$ is the space of polynomial functions of degree at most $p \geq 1$ on K . To obtain a form that is appropriate for discretization using the CDG method, we first write the governing equations (1) as a system of first order in space equations

$$\rho \frac{\partial^2 \mathbf{u}}{\partial t^2} - \nabla \cdot \boldsymbol{\sigma}(\mathbf{H})^T = \mathbf{b}, \quad \mathbf{H} - \nabla \mathbf{u} = \mathbf{0}. \quad (12)$$

Multiplying (12) by test functions $\mathbf{v}, \boldsymbol{\tau}$ and integrating by parts, our semi-discrete DG formulation is then expressed as: find $\mathbf{u}_h \in \mathcal{V}_h^p$ and $\mathbf{H}_h \in \Sigma_h^p$ such that for all $K \in \mathcal{T}_h$, we have

$$\int_K \rho \frac{\partial^2 \mathbf{u}_h}{\partial t^2} \cdot \mathbf{v} \, dx + \int_K \boldsymbol{\sigma}(\mathbf{H}_h)^T : \nabla \mathbf{v} \, dx - \oint_{\partial K} \widehat{\mathbf{t}}(\mathbf{H}_h) \cdot \mathbf{v} \, ds = \int_K \mathbf{b} \cdot \mathbf{v} \, ds, \quad \forall \mathbf{v} \in [\mathcal{P}_p(K)]^3, \quad (13)$$

$$\int_K \mathbf{H}_h : \boldsymbol{\tau} \, dx + \int_K \mathbf{u}_h \cdot (\nabla \cdot \boldsymbol{\tau}) \, dx - \oint_{\partial K} (\hat{\mathbf{u}}_h \otimes \mathbf{n}) : \boldsymbol{\tau} \, ds = \mathbf{0}, \quad \forall \boldsymbol{\tau} \in [\mathcal{P}_p(K)]^{3 \times 3}. \quad (14)$$

To complete the description we need to specify the numerical fluxes $\widehat{\mathbf{t}}(\mathbf{H}_h)$ and $\hat{\mathbf{u}}_h$ for all element boundaries ∂K . We use a formulation based on the CDG method [15], which is a slight modification of the LDG method [23] to obtain a compact and sparser stencil with improved stability properties. We describe the fluxes in a simplified form, where we implicitly set the LDG parameters $\mathbf{c}_{12} = -\mathbf{C}_{21} = \mathbf{n}/2$ and $C_{22} = 0$.

First, we introduce a *switch function* $S_K^{K'} \in \{-1, 1\}$ for each internal edge e that element K shares with a neighboring element K' . We require that $S_K^{K'} = -S_{K'}^K$, but unlike the standard LDG method no other restrictions are imposed. We use the simple *natural switch*, which is positive if the global element number of K is greater than that of K' , and negative otherwise.

The discretization is then performed as follows:

- (i) First, equation (14) is solved for each element K to obtain the gradients \mathbf{H}_h . This requires the definition of the numerical fluxes $\hat{\mathbf{u}}$, which is done using standard “up-winding” according to the switch function:

$$\hat{\mathbf{u}}_h = \begin{cases} \mathbf{u}'_h & \text{if } S_K^{K'} = +1 \\ \mathbf{u}_h & \text{if } S_K^{K'} = -1. \end{cases} \quad (15)$$

Here, \mathbf{u}'_h is the numerical solution defined by the neighboring element K' on the edge.

- (ii) The computed gradients \mathbf{H}_h are then used to compute the second term of (13), for each element K .
- (iii) It remains to define the numerical tractions $\widehat{\mathbf{t}}(\widehat{\mathbf{H}}_h)$ in the third term of (13) for each element K . This is done by first introducing the “edge gradients” \mathbf{H}_h^e for each edge e of K , using a slight modification of (14):

$$\int_K \mathbf{H}_h^e : \boldsymbol{\tau} dx + \int_K \mathbf{u}_h \cdot (\nabla \cdot \boldsymbol{\tau}) dx - \oint_{\partial K} (\hat{\mathbf{u}}_h^e \otimes \mathbf{n}) : \boldsymbol{\tau} ds = \mathbf{0}, \quad \forall \boldsymbol{\tau} \in [\mathcal{P}_p(K)]^{3 \times 3} \quad (16)$$

with

$$\hat{\mathbf{u}}_h^e = \begin{cases} \hat{\mathbf{u}}_h & \text{on edge } e, \text{ from equation (15),} \\ \mathbf{u}_h & \text{otherwise.} \end{cases} \quad (17)$$

These are then used to define the numerical tractions $\widehat{\mathbf{t}}(\widehat{\mathbf{H}}_h)$ on edge e :

$$\widehat{\mathbf{t}}(\widehat{\mathbf{H}}_h)^e = C_{11}(\mathbf{u}'_h - \mathbf{u}_h) + \begin{cases} \boldsymbol{\sigma}^T(\mathbf{H}_h^e)\mathbf{n} & \text{if } S_K^{K'} = +1 \\ \boldsymbol{\sigma}^T(\mathbf{H}_h^{e'})\mathbf{n} & \text{if } S_K^{K'} = -1, \end{cases} \quad (18)$$

where $\mathbf{H}_h^{e'}$ is the edge gradient from the neighboring element K' on edge e . Note that these fluxes can be seen as “down-winding” according to the switch function, and the parameter C_{11} is used for additional stabilization. In all our examples we set $C_{11} = 100/h$ where h is the smallest edge length of the element.

The procedure described above can be seen as a local elimination of the auxiliary variables \mathbf{H}_h , which results in a numerical scheme that can be considered a discretization of the original un-split form of the equations. Additional properties, including the sparsity pattern of the stencils, are discussed in [15].

3.1.2. Boundary conditions

At a boundary edge, we impose the conditions weakly through the fluxes $\hat{\mathbf{u}}$ and $\widehat{\mathbf{t}}(\widehat{\mathbf{H}}_h)$:

Dirichlet : At a prescribed displacement boundary (4), where $\mathbf{u} = \bar{\mathbf{u}}$, we set

$$\widehat{\mathbf{t}}(\widehat{\mathbf{H}}_h) = \boldsymbol{\sigma}^T(\mathbf{H}_h)\mathbf{n} - C_{11}(\mathbf{u}_h - \bar{\mathbf{u}}) \quad (19)$$

$$\hat{\mathbf{u}} = \bar{\mathbf{u}}, \quad (20)$$

with $C_{11} > 0$; we use the same value as on the internal edges, $C_{11} = 100/h$.

Neumann : At a prescribed stress boundary (5), with $\boldsymbol{\sigma}^T \mathbf{n} = \bar{\mathbf{t}}$, we set

$$\widehat{\mathbf{t}}(\widehat{\mathbf{H}}_h) = \bar{\mathbf{t}} \quad (21)$$

$$\hat{\mathbf{u}} = \mathbf{u}_h \quad (22)$$

Absorbing : At an absorbing boundary (6), we use the Neumann condition (21)-(22), with $\bar{\mathbf{t}} = \mathbf{Z} \frac{\partial \mathbf{u}}{\partial \bar{\mathbf{t}}}$.

3.1.3. Semi-discrete equations

The actual discretization procedure is carried out using a standard finite element technique. We define a set of equidistributed nodes \mathbf{x}_j , $j = 1, \dots, N$, within each element K , where for simplex elements $N = \binom{p+D}{D}$ in D spatial dimensions. We then determine the shape functions as the Lagrange interpolation functions $\phi_i(\mathbf{x}) \in \mathcal{P}_p(K)$ such that $\phi_i(\mathbf{x}_j) = \delta_{ij}$. Using these, the solution in each element can be written in terms of its discrete representation coefficients \mathbf{u}_i as:

$$\mathbf{u}_h(\mathbf{x}) = \sum_{i=1}^n \mathbf{u}_i \phi_i(\mathbf{x}) \quad (23)$$

and similarly for the auxiliary variable \mathbf{H}_h , the test functions $\mathbf{v}, \boldsymbol{\tau}$, and the time-derivatives $\partial \mathbf{u}_h / \partial t$. We evaluate all integrals in (13),(14) using high-order Gaussian quadrature rules, and setting the test function expansions coefficients to the identity matrix we obtain the semi-discrete form of our equations:

$$\mathbf{M} \frac{d^2 \mathbf{U}}{dt^2} = \mathbf{F} - \mathbf{K} \mathbf{U} - \mathbf{C} \frac{d \mathbf{U}}{dt}, \quad (24)$$

for solution vector $\mathbf{U} = [\mathbf{u}_i]$, mass matrix \mathbf{M} , stiffness matrix \mathbf{K} , damping matrix \mathbf{C} , and force vector \mathbf{F} . Because of the discontinuous spaces, \mathbf{M} is block diagonal and can therefore efficiently be inverted using block-wise LU factorizations. The stiffness matrix \mathbf{K} connects the elements, but only in a compact way such that each element is connected to its neighbors. The only contributions to the damping matrix \mathbf{C} come from the absorbing boundary conditions.

3.2. Temporal Discretization

We integrate (24) in time using a standard fourth order Runge-Kutta method. First, we rewrite it as a first-order system in time of twice the original size:

$$\frac{d}{dt} \begin{pmatrix} \mathbf{U} \\ \mathbf{V} \end{pmatrix} = \begin{pmatrix} \mathbf{V} \\ \mathbf{M}^{-1}(\mathbf{F} - \mathbf{K}\mathbf{U} - \mathbf{C}\mathbf{V}) \end{pmatrix} = \begin{pmatrix} \mathbf{0} & \mathbf{I} \\ -\mathbf{M}^{-1}\mathbf{K} & -\mathbf{M}^{-1}\mathbf{C} \end{pmatrix} \begin{pmatrix} \mathbf{U} \\ \mathbf{V} \end{pmatrix} + \begin{pmatrix} \mathbf{0} \\ \mathbf{M}^{-1}\mathbf{F} \end{pmatrix}. \quad (25)$$

We then set $\mathbf{Y} = \begin{pmatrix} \mathbf{U} \\ \mathbf{V} \end{pmatrix}$, and write (25) as $d\mathbf{Y}/dt = \mathbf{R}(\mathbf{Y})$. This system is integrated in time using the RK4 scheme, where the timestep from \mathbf{Y}^n to \mathbf{Y}^{n+1} is carried out as:

$$\begin{aligned} \mathbf{K}_1 &= \Delta t \cdot \mathbf{R}(\mathbf{Y}^n) \\ \mathbf{K}_2 &= \Delta t \cdot \mathbf{R}(\mathbf{Y}^n + \mathbf{K}_1/2) \\ \mathbf{K}_3 &= \Delta t \cdot \mathbf{R}(\mathbf{Y}^n + \mathbf{K}_2/2) \\ \mathbf{K}_4 &= \Delta t \cdot \mathbf{R}(\mathbf{Y}^n + \mathbf{K}_3) \\ \mathbf{Y}^{n+1} &= \mathbf{Y}^n + (\mathbf{K}_1 + 2\mathbf{K}_2 + 2\mathbf{K}_3 + \mathbf{K}_4)/6. \end{aligned} \quad (26)$$

For our wave-propagation problems, the timestep Δt needs to be small enough for accurate and stable solutions throughout the simulation, so we simply use a constant value instead of an adaptive scheme.

3.2.1. Axisymmetric form

For the axisymmetric form of the governing equations (7)-(8), with the stresses (9), we use a similar discretization procedure in the planar domain (r, z) for the solution components (u_r, u_z) . We note that the equations again can be written in the form (12), which can be discretized exactly as described above. The main two differences are:

- (i) The mass-matrix \mathbf{M} has an r -dependency (but it is still block-diagonal).
- (ii) The term $\sigma_{\theta\theta}$ is treated as a source term \mathbf{b} , which is a function of the gradients \mathbf{H}_h .

These two modifications are straight-forward and we omit the details.

4. Filter Diagonalization Method

To extract the resonance frequencies and their corresponding quality factors from the computed time-series, we use the filter diagonalization method [16,17] to perform a so-called harmonic inversion. Harmonic inversion begins with the classic problem of Prony [24], where one wishes to fit a time history to a sum of decaying harmonics (a Prony series):

$$y(t) \approx \sum_k d_k e^{-i\omega_k t}, \quad (27)$$

where the fitting parameters are (complex-valued) d_k and ω_k – the Q-factors and resonant modes being found directly from the ω_k s. Here $y(t)$ represents, the system's response measured at some location or is the mean response over a collection of locations. The problem is inherently non-linear and well known to be numerically sensitive. The first reasonably successful procedure is in fact due to Prony wherein one solves two linear algebra problems and a high order root finding problem to obtain a fit. Unfortunately, Prony's

method, like a number of intervening variants, is known to not be very robust or efficient. An alternate, well conditioned, and fully linear method of doing the same is to perform a Fourier transform of $y(t)$. In this case one ends up fixing the ω_k s at a spacing of $O(1/T)$, where T is the duration of the time history – thus rendering the problem linear but with limited frequency resolution.

Harmonic inversion via filter diagonalization circumvents the short comings of these earlier direct approaches. The method has its origins in the extraction of the eigenvalues of complex-symmetric Hamiltonians (in quantum mechanical systems) directly from auto-correlation functions measured and/or computed over short time intervals [16]. The details of the method are well described in [17] and we do not repeat them here. We only remark that the methodology permits one to compute complex-valued frequencies with a frequency resolution as a user specified parameter; in practice one chooses a (real-valued) frequency window of interest and a desired number of frequencies within this window. The procedure to find the (complex-valued) frequencies is local to this window and involves the solution of small generalized eigenvalue problems of the size of the number of desired eigenvalues in the (real-valued) frequency window. The procedure to generate these small problems is a cleverly designed Krylov method with a targeted resolution. These eigenproblems are best approached via a singular-value decomposition for maximum stability and accuracy. We perform our harmonic inversion using the freely available *harminv* software package [25] developed by Steven G. Johnson.

4.1. Excitation method

The input signal $P(t)$ should excite a broad spectrum of frequencies, but also be well-resolved by the time-integrator to minimize numerical artifacts. We use a Gaussian pulse of the form

$$P(t) = A \exp(-(t - \alpha w)^2/w^2), \quad (28)$$

where the maximum amplitude A is irrelevant since the equations are linear, and the time-width of the Gaussian is set to a fraction of the period of the desired frequency f_0 , $w = 0.01T_0 = 0.01/f_0$. Finally, the function is shifted a factor $\alpha = 6$ widths to obtain smooth time-profiles when our time integration starts at time $t = 0$.

At $t = 2\alpha w$ we assume the Gaussian has decayed out, and we integrate in time for an additional 150 periods T_0 . At a large number of equally spaced times t_i , $i = 1, \dots, N$. we compute an output quantity from the solution, which gives the time series $y_i = y(t_i)$ that we will use to determine the spectral properties of the resonator.

4.2. Practical procedure

Using the *harminv* software is straight-forward, and here we simply discuss some of the parameters and the procedure that we use to run it.

- When building the time-series, we store enough samples N so that the desired frequencies are well-resolved. In our simulations, this corresponds to $N \approx 10,000$, or every 200th Runge-Kutta timestep.
- While we know a close approximation to the resonant frequency f_0 , we have found that the results are better if we specify a very broad frequency range to *harminv*, about three magnitudes below and three magnitudes above the desired frequency.
- The default values are used for all optional *harminv* parameters.
- From the list of modes computed by *harminv*, we find the one closest to the desired frequency, and extract its frequency and corresponding Q-factor.

5. Examples

All our simulations have been done using the 3DG software [26], which is a general purpose framework for discontinuous and continuous Galerkin discretization. It supports arbitrary systems of conservation laws, elements of any polynomial degree, and fully unstructured simplex meshes. The solvers include both explicit

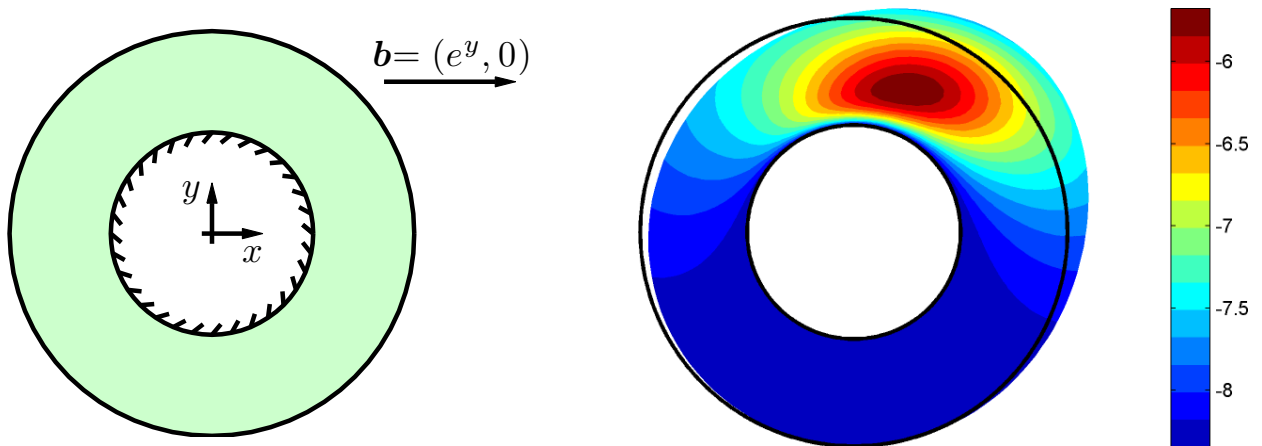


Fig. 2. Left: The annulus test problem. Right: The steady-state solution, on a deformed mesh with pressure color contours.

and implicit time integrators, steady-state nonlinear solvers, and eigenvalue solvers for linearized problems. Linear solvers include direct sparse solvers as well as multigrid/ILU preconditioned Krylov subspace methods. The time-integrators are fully parallelized using MPI for distributed parallel computers. In this work we use the serial solvers for all planar problems and the parallel ones for the three dimensional computations.

5.1. Convergence Study for Annulus Problem

First we validate the accuracy of our DG formulation using a plane strain test problem. We consider an annulus with inner radius 1 and outer radius 2 (see Fig. 2, left) and material properties $E = 10$, $\nu = 0.3$, and $\rho = 1.0$. The boundary $\partial\Omega_u$ at the inner circle is clamped ($\mathbf{u} = 0$), the boundary $\partial\Omega_\sigma$ at the outer circle is stress free ($\boldsymbol{\sigma} = 0$), and a distributed area force $\mathbf{b} = (e^y, 0)$ is acting on the body. The steady-state (i.e. static) solution to the problem is shown in Fig. 2, right, as a deformed mesh plot with pressure contours.

As output quantity for our error calculations, we study the average x -displacement along the outer circle:

$$\bar{u}_x(\mathbf{u}) = \int_{\partial\Omega_\sigma} u_x ds / \int_{\partial\Omega_\sigma} ds. \quad (29)$$

5.1.1. Spatial Convergence

To demonstrate the spatial accuracy and order of convergence of the scheme, we compute steady-state solutions of the annulus problem for a series of uniformly refined structured meshes and polynomial degrees $p = 1, \dots, 4$. The coarsest mesh has one single layer of triangular elements across the thickness and a total of 8 triangles, we refer to this element size as $h = 1$. Each triangle is then repeatedly split into 4 triangles, to produce a series of meshes with element sizes $h_r = 1/2^r$, $r = 0, \dots, 5$. To curve the elements (for $p > 1$), we generate a uniform grid of points within each element using cylindrical coordinates, and interpolate with isoparametric elements of degree p . An example mesh is shown in Fig. 3, left, corresponding to $r = 2$ refinements and polynomial degree $p = 3$.

We discretize the equations in space using 3DG, solve the resulting linear equations with a direct sparse solver, and compute \bar{u}_x for each mesh and polynomial degree. We consider the output on the finest mesh ($h_5 = 1/32$, $p = 4$) the “exact value” $\bar{u}_{x,\text{exact}}$. Figure 3, right, shows the errors $|\bar{u}_x - \bar{u}_{x,\text{exact}}|$ versus the element size h in a log-log diagram. We note that the slopes are close to the expected $p + 1$ order of convergence, except possibly for the $p = 2$ case which seems to have one order higher than this, perhaps because of symmetries in our test problem.

5.1.2. Temporal Convergence and Energy Conservation

It is expected that our explicit Runge-Kutta solver RK4 will solve our linear ODEs (25) with fourth order convergence in the convergent regime, but for validation of our code we show that this is indeed the case for

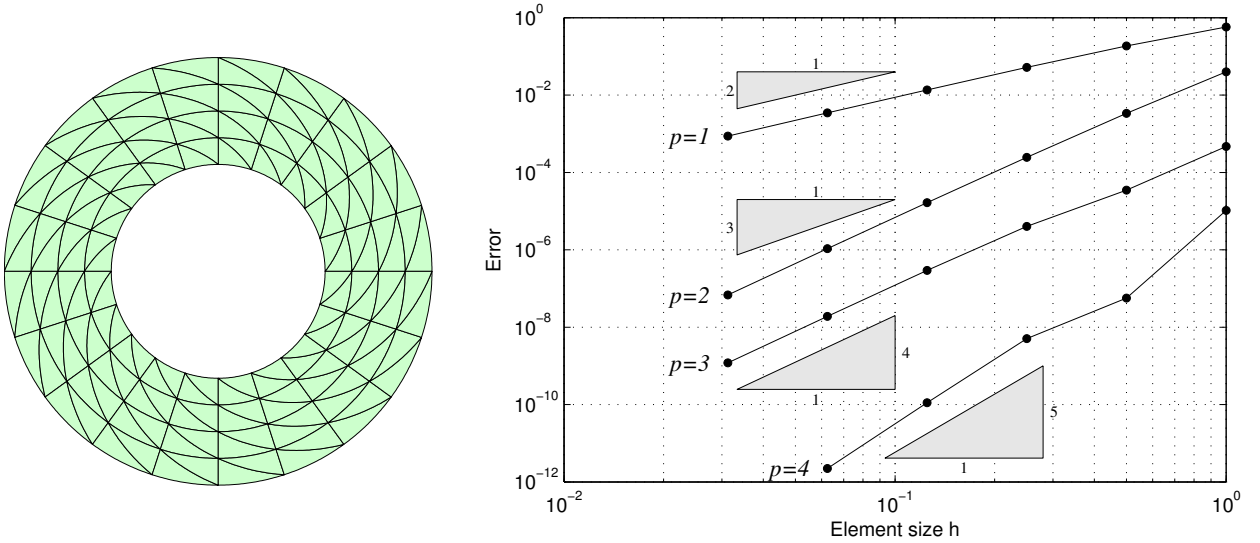


Fig. 3. Spatial convergence of the annulus problem, for a series of uniformly refined meshes and polynomial degrees $p = 1, \dots, 4$.

Δt	\bar{u}_x	Error $\bar{u}_x - \bar{u}_{x,\text{exact}}$	Order
$2 \cdot 10^{-3}$	-0.124403438817693	$1.8431338 \cdot 10^{-7}$	
$1 \cdot 10^{-3}$	-0.124403440548911	$0.1119159 \cdot 10^{-7}$	4.04
$5 \cdot 10^{-4}$	-0.124403440654328	$0.0064994 \cdot 10^{-7}$	4.11
$2.5 \cdot 10^{-4}$	-0.124403440660827		

Table 1

Temporal convergence for the annulus problem, showing the errors in \bar{u}_x at time $T = 10$ for a range of timesteps Δt .

our annulus problem with the typical spatial discretization of 3 uniform refinements and polynomial degrees $p = 4$. To obtain smooth solutions in time, we multiply the body forces by a Gaussian profile in time:

$$\mathbf{b}(t) = \begin{pmatrix} \exp(-(t-1)^2/0.1^2)e^y \\ 0 \end{pmatrix}, \quad (30)$$

and integrate until $T = 10$ using RK4 with four different timesteps. Again we study the output quantity \bar{u}_x , but computed at time T , and we use the value for the smallest timestep as our “exact value” $\bar{u}_{x,\text{exact}}$ (this time it is considered the exact solution in time, not space). The results are shown in Table 1, together with estimated orders of convergence for each refinement in time. The results clearly show the fourth order convergence rate in time.

We also note that our scheme very accurately conserves the total energy of the system. In Fig. 4, we plot the potential, the kinetic, and the total energy as a function of time, for the same problem as above with the largest considered timestep $\Delta t = 2 \cdot 10^{-3}$. After the Gaussian input (30) has decayed, the total energy stays very close to constant (the total relative loss at time $T = 10$ is about 10^{-9}).

5.2. Axisymmetric Disk Resonator

Our second example is the axisymmetric resonator presented in [27], which we use to validate our DG formulation with previous results and to demonstrate the feasibility of the time-domain approach. Since the problem is planar in the computational axisymmetric space, the resulting linear systems are relatively small and we can easily compute the true resonance modes using a sparse eigenvalue solver to compare with the results from harmonic inversion.

The geometry of the resonator is shown in Fig. 5, together with the unstructured triangular mesh. The radius of the disk is $R_d = 41.5 \mu\text{m}$, and it is supported on a conical post with upper radius $1.49 \mu\text{m}$, lower

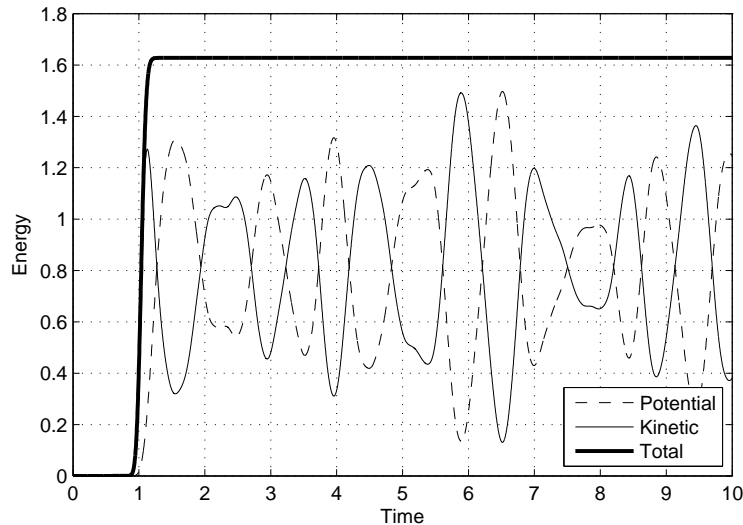


Fig. 4. Energy conservation for the time-integrated annulus problem with a Gaussian body force.

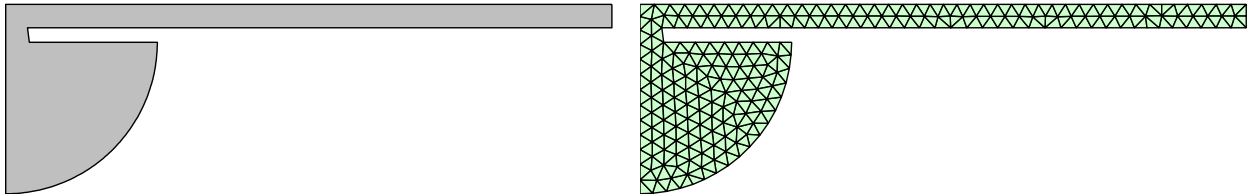


Fig. 5. Left: The axisymmetric disk resonator geometry, for the film thickness $1.6 \mu\text{m}$ and the substrate radius $R_s = 10.375 \mu\text{m}$. Right: Our unstructured mesh for the resonator.

radius $1.49 \mu\text{m}$, and nominal height $1 \mu\text{m}$. The material has a density of 4127 kg/m^3 , Poisson's ratio of 0.28 , and a Young's modulus of 139 GPa . We will vary the film thickness between $1.2 \mu\text{m} - 1.8 \mu\text{m}$. The semi-infinite substrate is approximated by a half-sphere of radius R_s , which we set to $R_d/4 = 10.375 \mu\text{m}$.

The motion is driven by a uniform radial pressure along the disk edge. For the output quantity in the time-domain computations, we use the average radial displacement \bar{u}_r , along the edge of the disk, similar to the annulus problem above. We will study the lowest radial eigenmode, with a frequency that can be approximated analytically as [28]:

$$f_0 = 2.04 \frac{c_o}{R_d} = 47.36 \text{ MHz}, \quad (31)$$

where $c_o = 6045 \text{ m/s}$.

Our test is a reproduction of the film thickness parameter study from [27] and the comparison with experimental values. We sweep the film thickness between $1.2 \mu\text{m}$ and $1.8 \mu\text{m}$, and compute the resonance frequency and corresponding quality factor for each case. The mesh has element sizes of about $0.5 \mu\text{m}$, which gives a total of 364 triangles. Within each element we use polynomials of degree $p = 4$, which gives a total of 3640 high-order nodes, or $10,920$ degrees of freedom (see Fig. 5, right).

First, we solve each case using the sparse eigenvalue solver and the approximate resonance frequency f_0 as shift. The resulting quality factors are shown as the blue solid curve in Fig. 6. We note that the results agree very well with the previous study, and again there is good agreement with the five experimental data points (despite our simple radiation boundary condition). Furthermore, we can see the very high sensitivity of the quality factor with respect to the film thickness.

Next, we show that the quality factors can also be obtained using explicit time-integration and harmonic inversion, and that the results are accurate. For this, we use the RK4 scheme (26) on our system with a timestep of $\Delta t = 1.6 \cdot 10^{-12}$. We note that this is about half of the largest timestep that satisfies the CFL

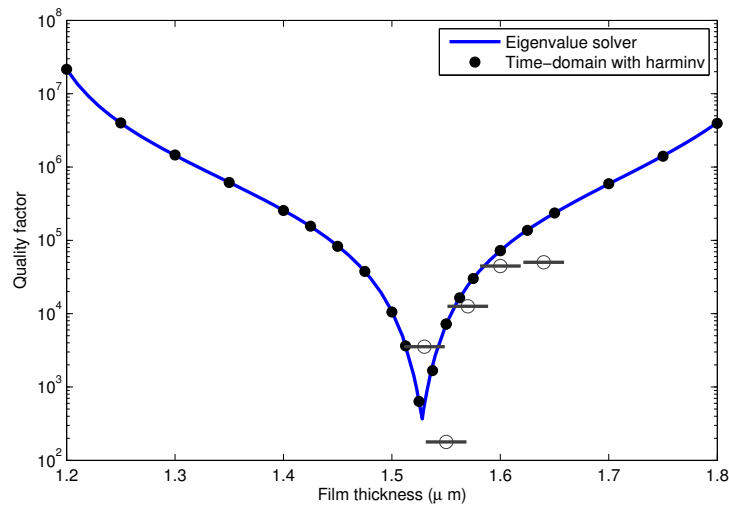


Fig. 6. Quality factors as function of the film thickness for the axisymmetric disk resonator, corresponding to the resonance frequency closest to the shift $f_0 = 47.36$ MHz. The solid blue curve is the eigenvalue calculations, and the black dots are the predictions using harminv and the time series data. The gray open circles with error bars indicated measured experimental values [29].

condition, but we have found that the largest quality factors ($> 10^6$) require somewhat smaller timesteps to be accurately predicted. As described in Sec. 4, we use a Gaussian pressure function at the disk edge, with amplitude $A = P_0 = 10^6$ Pa. We integrate until time $T = 150T_0 = 3.17 \cdot 10^{-6}$ sec, which corresponds to almost 2 million timesteps. At every 200th step we compute the output quantity, which is the average radial displacement $\bar{u}_r(t)$ along the edge of the disk, for a total time series length of almost 10,000.

Using the procedure described before, we perform the filter diagonalization and extract the mode closest to f_0 . The corresponding Q-factors are shown as black dots in Fig. 6, which shows an excellent agreement with the eigenvalue calculations.

We point out that for this case, the eigenvalue calculations were between one and two magnitudes faster than the proposed time-domain approach, mainly because of the large number of timesteps required. However, the main point is that the computational cost for the explicit time-stepping will scale well for large three dimensional problems, for which the eigenvalue calculations become increasingly harder (or virtually impossible) to solve.

5.3. 3-D Disk Resonator

Next, we demonstrate the accuracy and scaling of our method on a fully three dimensional problem. We consider the same disk resonator as above, but without the axisymmetric assumption. Our fully unstructured mesh consists of about 18,000 tetrahedra, which for our polynomial degree $p = 3$ gives about 350,000 high-order nodes, or 2 million degrees of freedom (see Fig. 7, left). For simplicity we only consider one of the film thicknesses, $1.6\mu m$.

We run the problem using the parallel Runge-Kutta solver in 3DG, which is a standard domain decomposition explicit timestepping method with overlapping communication/computations. The scaling as a function of the number of processes is close to perfect for large problems, partly due to the relatively large stencil of high-order DG methods [30]. We use a matrix-based solver and the entire time integration is essentially done by matrix-vector products.

We use similar data to the axisymmetric problem: $\Delta t = 1.6 \cdot 10^{-12}$, same driving force applied radially on the edge of the disk, and same total number of timesteps. The resonance frequency predicted by harminv is 47.2102 MHz, which agrees very well with the value 47.2103 MHz from the axisymmetric computations. The corresponding quality factor is $72.1 \cdot 10^3$, which is close to the value $72.4 \cdot 10^3$ from the axisymmetric

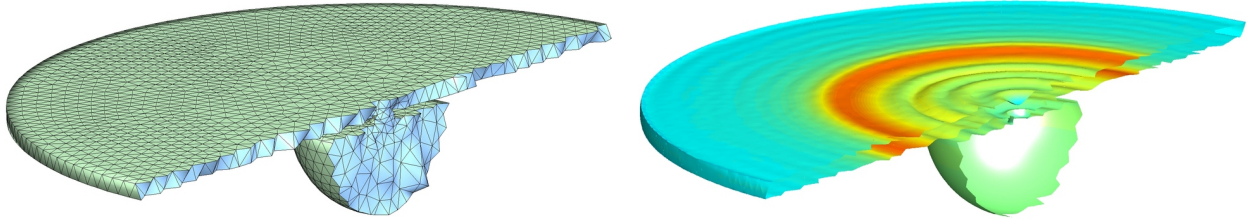


Fig. 7. The 3-D disk resonator simulation. Left: The fully unstructured tetrahedral mesh, with 18,000 elements and 350,000 high order nodes. Right: A sample solution, with radial component of displacement as color contours.

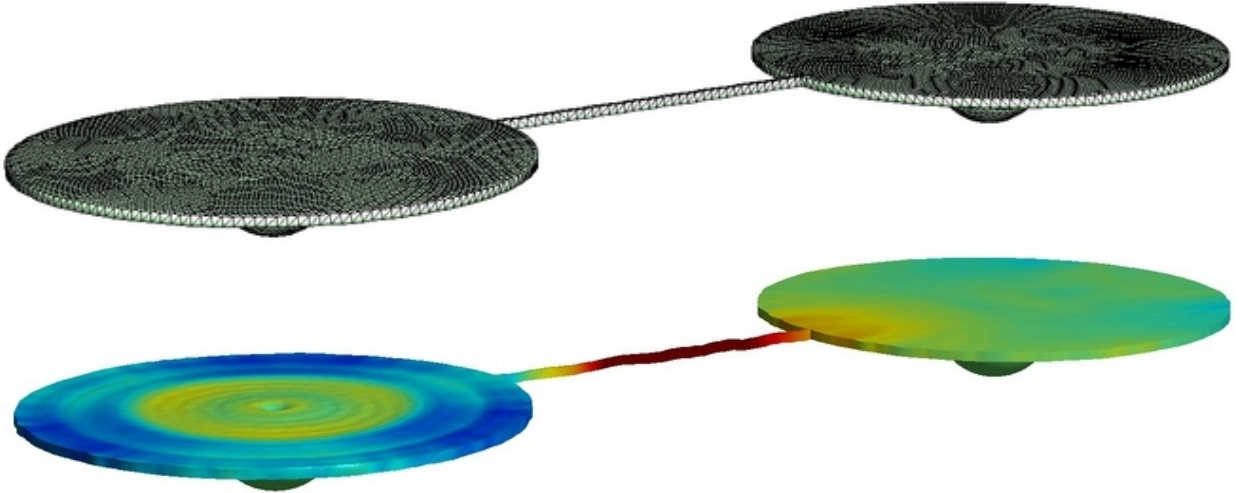


Fig. 8. The 3-D double disk resonator simulation, unstructured tetrahedral mesh (top) and a sample solution (bottom), with deformed mesh and radial component of displacement as color contours.

case; the deviations are likely due to the approximate radiation boundary condition.

5.4. 3-D Double Disk Resonator

As our final example, we simulate a double disk resonator consisting of two identical disks connected by a coupling beam. The length of the beam is half of the dominant longitudinal wavelength, or

$$L = \frac{\lambda_1}{2} = \frac{1}{2f_0} \sqrt{\frac{E}{\rho}} = 61.5 \mu m \quad (32)$$

The problem is slightly more than twice as large as the single disk resonator, or 764,000 high-order nodes and a total of 4.58 million degrees of freedom (Fig. 8, top). With this example we wish to demonstrate the following:

- (i) A truly 3-D case that cannot be well approximated by the axisymmetric formulation.
- (ii) That even for relatively simple geometries like this, fully automated tetrahedra mesh generators are essential.
- (iii) Our methods scale perfectly, in the sense that the simulation time for the double disk resonator is only twice as long as for a single disk.

In this case, we drive the resonator by applying a radial force on the edge of the left disk (except at the small region where the beam is attached). Our time series are constructed by computing the average radial displacement along the edge of the right disk (again excluding the region with the beam). All other simulation parameters are identical to before; a typical solution is shown in Fig. 8 (bottom). The main reason for coupling two disks in this way is to keep the high quality factor but increase the sensing area. In

Problem	Single Disk	Double Disk
# tetrahedra	17,873	38,186
Polynomial degree	$p = 3$	$p = 3$
Total DOFs	2.14 million	4.58 million
Time per 1,000 RK steps		
4 nodes, 96 cores	41.2s	87.5s
8 nodes, 192 cores	21.6s	45.3s
16 nodes, 384 cores	11.5s	23.5s
32 nodes, 768 cores	6.4	12.7s

Table 2

Compute times for the two 3-D problems. We note that the problems scales linearly, in the sense that the double disk requires about twice the compute time as the single, and that doubling the number of processors essentially reduces the time by a factor of 2.

our simulation, `harminv` predicts a strong resonance at 47.2104 MHz with quality factor $72.4 \cdot 10^3$, which are very close to the single disk results.

To verify our claims about the perfect scaling, we compare the computation times for the single and the double disk in Table 2. We note that the scaling is actually somewhat better than linear (less than twice the time for more than twice the number of unknowns). The reason for this is that we keep the number of computational processes fixed and increase the size of the system (so-called *strong* scaling studies are done by doing the opposite). Therefore, the number of elements in each partition is higher for the larger problem, which in turn results in less overhead and a more efficient parallelization.

6. Conclusions

We have presented a time-domain approach for prediction of resonant frequencies and quality factors for mechanical resonators. Unlike frequency-based approaches, its computational cost is essentially proportional to the size of the problem, and the explicit time-integration scales very well on large parallel computers. To allow for high-order accuracy on fully unstructured tetrahedral meshes, we use a second-order Discontinuous Galerkin discretization in space, inspired by the Compact DG method. The semi-discrete system is written in first-order form and integrated in time using a standard fourth-order Runge-Kutta method.

To extract the resonance properties of the system from the time-domain simulations, we apply a broadband Gaussian pulse and measure an appropriate output quantity for several oscillation periods. The filter diagonalization method of Wall and Neuhauser[16] in the modified form of Mandelshtam and Taylor[17] (via `harminv`[25]), is then used to analyze the time series. We show how the approach accurately predicts the quality factors of a single disk resonator for a range of film thicknesses. We also demonstrate the excellent scaling, by solving a coupled double disk resonator in approximately twice the time as the single disk.

In summary, we conclude that the methodology proposed, viz. high-order explicit time integration with high-order Discontinuous Galerkin in space (appropriately expressed for linear elasticity) in conjunction with filter diagonalization, yields a scalable scheme for accurately computing quality factors in resonant MEMS structures.

7. Acknowledgment

This material is based upon work supported by the National Science Foundation under Award No. CMMI-0928785, by the Air Force Office of Scientific Research, USAF, under grant/contract number FA9550-10-1-0229, and by the Director, Office of Science, Computational and Technology Research, U.S. Department of Energy under Contract No. DE-AC02-05CH11231.

References

- [1] K. Graff, Wave Motion in Elastic Solids, Oxford University Press, 1975.

- [2] J. Lysmer, R. Kuhlemeyer, Finite dynamic model for infinite media, *Journal of the Engineering Mechanics Division, ASCE* 95 (1969) 859–877.
- [3] W. Chew, Q. Liu, Perfectly Matched Layers for Elastodynamics: A New Absorbing Boundary Condition, *Journal of Computational Acoustics* 4 (1996) 341–359.
- [4] F. Hastings, J. Schneider, S. Broschat, Application of the perfectly matched layer (PML) absorbing boundary condition to elastic wave propagation, *Journal of the Acoustical Society of America* 100 (1996) 3061–3069.
- [5] F. Collino, C. Tsogka, Application of the perfectly matched absorbing layer model to the linear elastodynamic problem in anisotropic heterogeneous media, *Geophysics* 66 (2001) 294–307.
- [6] U. Basu, A. Chopra, Perfectly matched layers for transient elastodynamics of unbounded domains, *International Journal for Numerical Methods in Engineering* 59 (2004) 1039–1074.
- [7] Y.-H. Park, K. Park, High-Fidelity Modeling of MEMS Resonators Part I: Anchor Loss Mechanisms Through Substrate, *Journal of Microelectromechanical Systems* 13 (2004) 238–247.
- [8] D. Bindel, S. Govindjee, Elastic PMLs for resonator anchor loss simulation, *International Journal for Numerical Methods in Engineering* 64 (2005) 789–818.
- [9] T. Koyama, Efficient evaluation of damping in resonant mems, Ph.D. thesis, University of California, Berkeley (2008).
- [10] G. Sleijpen, A. Booten, D. Fokkema, H. V. der Vorst, Jacobi-Davidson Type Methods for Generalized Eigenproblems and Polynomial Eigenproblems, *BIT* 36 (1996) 595–633.
- [11] G. Sleijpen, H. van der Vorst, A Jacobi-Davidson Iteration Method for Linear Eigenvalue problems, *SIAM Review* 42 (2000) 267–293.
- [12] P. Arbenz, M. Hochstenbach, A Jacobi-Davidson method for solving complex symmetric eigenvalue problems, *SIAM Journal on Scientific Computing* 25 (2004) 1655–1673.
- [13] S.-S. Li, Y.-W. Lin, Z. Ren, C. T.-C. Nguyen, An msi micromechanical differential disk-array filter, in: *Dig. of Tech. Papers, 14th Int. Conf. on Solid-State Sensors & Actuators (Transducers 07)*, 2007, pp. 307–311.
- [14] B. Cockburn, C.-W. Shu, Runge-Kutta discontinuous Galerkin methods for convection-dominated problems, *Journal of Scientific Computing* 16 (2001) 173–261.
- [15] J. Peraire, P.-O. Persson, The compact discontinuous Galerkin (CDG) method for elliptic problems, *SIAM Journal on Scientific Computing* 30 (2008) 1806–1824.
- [16] M. Wall, D. Neuhauser, Extraction, through filter-diagonalization, of general quantum eigenvalues or classical normal mode frequencies from a small number of residues or a short-time segment of a signal. I. Theory and application to a quantum-dynamics model, *Journal of Chemical Physics* 102 (1995) 8011–8022.
- [17] V. Mandelshtam, H. Taylor, Harmonic inversion of time signals and its applications, *Journal of Chemical Physics* 107 (1997) 6756–6769.
- [18] S. J. Owen, A survey of unstructured mesh generation technology, in: *Proceedings of the 7th International Meshing Roundtable, Sandia Nat. Lab.*, 1998, pp. 239–267.
- [19] P.-O. Persson, G. Strang, A simple mesh generator in Matlab, *SIAM Review* 46 (2004) 329–345.
- [20] J. Peraire, K. Morgan, Unstructured mesh generation including directional refinement for aerodynamic flow simulation, *Finite Elements in Analysis & Design* 25.
- [21] L. A. Freitag, C. Ollivier-Gooch, Tetrahedral mesh improvement using swapping and smoothing, *International Journal for Numerical Methods in Engineering* 40 (1997) 3979–4002.
- [22] P.-O. Persson, J. Peraire, Curved mesh generation and mesh refinement using Lagrangian solid mechanics, in: *47th AIAA Aerospace Sciences Meeting and Exhibit, Orlando, Florida, 2009, AIAA-2009-949*.
- [23] B. Cockburn, C.-W. Shu, The local discontinuous Galerkin method for time-dependent convection-diffusion systems, *SIAM Journal on Numerical Analysis* 35 (1998) 2440–2463 (electronic).
- [24] R. Prony, Essai expérimental et analytique sur les lois de la dilatabilité des fluides élastiques, et sur celles de la force expansive de la vapeur de l’eau et de la vapeur de l’alkool, á différentes températures, *Journal de L’École Polytechnique* 1 (1795) 24–76.
URL <http://gallica.bnf.fr>
- [25] S. Johnson, Harminv (ver. 1.3.1) (2004).
URL <http://ab-initio.mit.edu/wiki/indep.php/Harminv>
- [26] J. Peraire, P.-O. Persson, Adaptive High-Order Methods in Computational Fluid Dynamics, Vol. 2 of *Advances in Computational Fluid Dynamics*, World Scientific Publishing Co., 2011, Ch. 5 – High-Order Discontinuous Galerkin Methods for CFD.
- [27] D. S. Bindel, S. Govindjee, Elastic PMLs for resonator anchor loss simulation, *International Journal for Numerical Methods in Engineering* 64 (2005) 789–818.
- [28] S. Govindjee, Estimation of the fundamental mode of a radial-disk resonator, Tech. Rep. UCB/SEMM-2011/02, University of California Berkeley, Department of Civil Engineering (2011).
- [29] D. S. Bindel, E. Quévy, T. Koyama, S. Govindjee, J. Demmel, R. Howe, Anchor loss simulation in resonators, in: *Proceedings of MEMS 2005, IEEE*, 2005, pp. 133–136.
- [30] P.-O. Persson, Scalable parallel Newton-Krylov solvers for discontinuous Galerkin discretizations, in: *47th AIAA Aerospace Sciences Meeting and Exhibit, Orlando, Florida, 2009, AIAA-2009-606*.